World Journal of Mathematics and Physics
Print ISSN: 2960-009X
Online ISSN: 2960-0103
DOI: https://doi.org/10.61784/wjmp3019

MORPHOLOGY-CONTROLLED SYNTHESIS OF OCTAHEDRAL NIXFE1-X@C COMPOSITES DERIVED FROM BIMETALLIC MOFS FOR ENHANCED MICROWAVE ABSORPTION

YingJie Song*, ZhenHua Shi
Department of Physics, School of Sciences, Xi'an Technological University, Xi'an 710021, Shaanxi, China.
**Corresponding Author: YingJie Song*

Abstract: Carbonaceous materials derived from metal-organic frameworks (MOFs) have attracted significant attention as potential electromagnetic wave absorbers due to their tunable structures, high porosity, and large specific surface areas. In this study, a facile strategy was developed to control the morphology of Ni_xFe_{1-x}-MOFs by adjusting the Ni/Fe molar ratio in the precursors. Specifically, a near-octahedral Ni_xFe_{1-x}-MOF structure was successfully synthesized at a Ni/Fe molar ratio of 0.5:0.5. Following pyrolysis at 600°C in a nitrogen atmosphere, porous Ni_xFe_{1-x}@C composites were obtained. The $Ni_{0.5}Fe_{0.5}$@C composite exhibited significantly enhanced microwave absorption performance. At a matching thickness of 1.94 mm, the maximum reflection loss (RL) reached -81.35 dB at 13.8 GHz, with a corresponding effective absorption bandwidth (EAB, RL < -10 dB) of 5.3 GHz (ranging from 11.7 to 17.0 GHz). The superior microwave absorption properties are attributed to the improved impedance matching, multiple polarization relaxations, and conduction losses facilitated by the unique octahedral structure. This research provides a novel approach for the fabrication of high-performance electromagnetic wave absorbing materials through the compositional regulation of bimetallic MOF precursors.
Keywords: Microwave absorption properties; Metal-Organic Frameworks (MOFs); NiFe impedance matching

1 INTRODUCTION

Over the past few decades, the continuous advancement of information technology and the ubiquitous use of electronic devices have led to severe electromagnetic pollution [1-5]. Microwave absorption (MA) materials are capable of absorbing and attenuating unwanted electromagnetic waves by converting them into heat energy that is then dissipated. Consequently, there is an ever-increasing demand for high-performance microwave absorbing materials. To satisfy the spatial constraints of practical applications and achieve effective electromagnetic wave absorption across various electronic platforms, materials characterized by thin thickness and strong absorption capacity have emerged as a primary research focus [6-8].

Metal-organic frameworks (MOFs), composed of metal ions and organic ligands, are considered among the most promising candidates for electromagnetic wave (EMW) absorption materials due to their tunable structures, high porosity, and large specific surface areas [9-14]. Benefiting from these advantages, MOF-derived EMW absorption materials exhibit excellent electrical conductivity, favorable magnetic properties, and abundant interfacial defects, which contribute to optimized impedance matching and enhanced electromagnetic loss [15-19]. Generally, MOFs can be categorized into monometallic and bimetallic MOFs based on their metallic composition. Compared with monometallic MOFs, bimetallic MOFs offer greater flexibility and effectiveness in modulating their morphology and resultant magnetic properties by varying the metal molar ratios. This tunability and the synergistic effect of multiple loss mechanisms provide significant potential for tailoring electromagnetic parameters to achieve superior impedance matching and high EMW attenuation, thereby enhancing microwave absorption performance [20-22]. For instance, Wang et al. synthesized CoFe-MOF nanocomposites with diverse structures by adjusting the Co/Fe molar ratio [23]. The integration of multicomponents, abundant defects, and unique crystalline structures significantly improved their performance, demonstrating the vast potential of bimetallic MOF derivatives in the field of EMW absorption [24].

Herein, we report a facile approach to control the morphology of porous Ni_xFe_{1-x}@C composites by simply adjusting the Ni/Fe molar ratio in the Ni_xFe_{1-x}-MOF precursors. Following pyrolysis at 600°C in a nitrogen atmosphere, the resulting Ni_xFe_{1-x}@C composites were obtained. Notably, the composite with a Ni/Fe molar ratio of 0.5:0.5 exhibited significantly enhanced comprehensive microwave absorption performance, which is primarily attributed to the optimized impedance matching and superior attenuation capacity facilitated by its unique structure. This work undoubtedly provides a valuable reference for the design and fabrication of novel electromagnetic wave absorbing materials.

2 EXPERIMENTAL

2.1 Materials

Nickel nitrate hexahydrate ($Ni(NO_3)_2·6H_2O$), ferric nitrate nonahydrate ($Fe(NO_3)_3·9H_2O$), DMF, and H_3BTC were purchased from Shanghai Aladdin Bio-Chem Technology Co. Ltd. All chemicals were used as received without further purification.

2.2 Preparation of NiFe-MOF

Ni_xFe_{1-x}-MOF were synthesized via a solvothermal method. To investigate the influence of different Ni/Fe ratios on the structure and morphology of the MOFs, the molar ratios of Ni to Fe in the initial salt solutions were set at 0.2:0.8(x=0.2), 0.4:0.6(x=0.4), 0.5:0.5(x=0.5), 0.6:0.4(x=0.6), and 0.8:0.2(x=0.8). The detailed procedure is as follows: First, specified molar amounts of $Ni(NO_3)_2·6H_2O$, $Fe(NO_3)_3·9H_2O$, and 210 mg of H_3BTC were dissolved in 30 mL of DMF and stirred for 30 min to obtain a homogeneous solution. The resulting mixture was then transferred into a Teflon-lined stainless steel autoclave and placed in an electric thermostatic drying oven. After being maintained at 170 °C for 24 h, the product was washed three times with absolute ethanol and dried in a vacuum oven at 60 °C for 12 h to yield the Ni_xFe_{1-x}-MOF.

2.3 Preparation of Ni_xFe_{1-x}@C composites

To transform the Ni_xFe_{1-x}-MOF precursors into Ni_xFe_{1-x}@C composites, the dried precursors were heated to 600 °C at a heating rate of 2 °C/min and maintained for 2 h under a nitrogen atmosphere. The resulting black powder derivatives of Ni_xFe_{1-x}-MOF(x=0.2, 0.4, 0.5, 0.6, and 0.8) were obtained and denoted as $Ni_{0.2}Fe_{0.8}$@C, $Ni_{0.4}Fe_{0.6}$@C, $Ni_{0.5}Fe_{0.5}$@C, $Ni_{0.6}Fe_{0.4}$@C, and $Ni_{0.8}Fe_{0.2}$@C, respectively.

2.4 Characterization

The morphology of the samples was observed using a field-emission scanning electron microscope (FESEM) equipped with an energy-dispersive X-ray spectrometer (EDS). The phase structures of the Ni_xFe_{1-x}@C composites were analyzed by X-ray diffraction (XRD) using Cu Kα radiation in the 2θ range of 30–100° and Raman spectroscopy. The elemental distribution and chemical valence states of the resulting products were investigated via X-ray photoelectron spectroscopy (XPS). The electromagnetic parameters of the Ni_xFe_{1-x}@C composites were measured using a vector network analyzer (VNA) via the coaxial method. The reflection loss (RL) of the samples was calculated based on the transmission line theory [25-26]:

$$RL = 20\,log\left|\frac{Z_{in} - Z_0}{Z_{in} + Z_0}\right| \quad (1)$$

where Z_0 and Z_{in} represent the characteristic impedance of free space and the input impedance of the absorber, respectively.

3 RESULT AND DISCUSSION

In this study, Ni_xFe_{1-x}-MOFs with various structures and their corresponding Ni_xFe_{1-x}@C composites were controllably synthesized by simply adjusting the Ni/Fe molar ratio. The micromorphologies of the Ni_xFe_{1-x}-MOF and Ni_xFe_{1-x}@C samples were characterized using SEM. Figures 1(a–e) present the SEM images of the Ni_xFe_{1-x}-MOF before annealing, corresponding to $Ni_{0.2}Fe_{0.8}$-MOF, $Ni_{0.4}Fe_{0.6}$-MOF, $Ni_{0.5}Fe_{0.5}$-MOF, $Ni_{0.6}Fe_{0.4}$-MOF, and $Ni_{0.8}Fe_{0.2}$-MOF, respectively. Figures 2(f–j) show the results for the corresponding Ni_xFe_{1-x}@C composites. As observed, the particles exhibit irregular spherical shapes at high Fe content. With the decrease in Fe content, the morphology evolves into polyhedral structures, followed by near-octahedral structures, and finally transitions into complex polyhedral structures, and at the same time, the particle size also decreases. Specifically, $Ni_{0.2}Fe_{0.8}$-MOF and $Ni_{0.4}Fe_{0.6}$-MOF displays a polyhedral structure with a size of approximately 15 μm and 10 μm. Samples $Ni_{0.5}Fe_{0.5}$-MOF and $Ni_{0.6}Fe_{0.4}$-MOF exhibit octahedral structures, with average sizes of approximately 7 μm and 5 μm, respectively. $Ni_{0.8}Fe_{0.2}$-MOF shows a complex polyhedral structure with a smaller particle size of about 1.5 μm. After annealing, the particle morphology remains largely unchanged, although the surfaces become noticeably rougher due to the formation of crystalline grains during the high-temperature heat treatment. Figure 2 displays the SEM elemental mapping results for the $Ni_{0.5}Fe_{0.5}$@C sample, confirming the uniform distribution of Ni, Fe, and C elements within the composite.

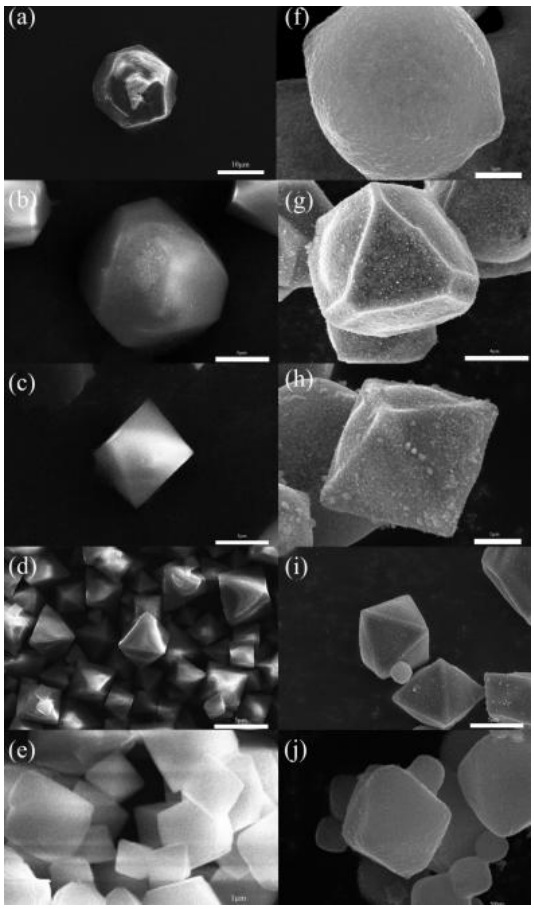

Figure 1 The SEM Images of (a-e) Correspond to $Ni_{0.2}Fe_{0.8}$-MOF, $Ni_{0.4}Fe_{0.6}$-MOF, $Ni_{0.5}Fe_{0.5}$-MOF, $Ni_{0.6}Fe_{0.4}$-MOF , and $Ni_{0.8}Fe_{0.2}$-MOF, (f-j) correspond to $Ni_{0.2}Fe_{0.8}$@C, $Ni_{0.4}Fe_{0.6}$@C, $Ni_{0.5}Fe_{0.5}$@C, $Ni_{0.6}Fe_{0.4}$@C, and $Ni_{0.8}Fe_{0.2}$@C

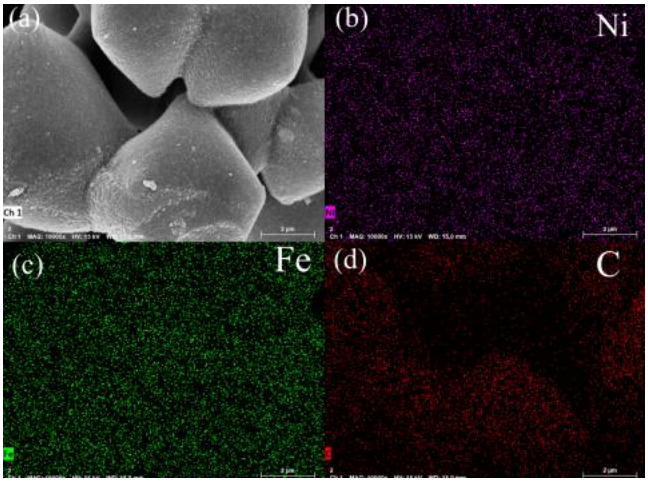

Figure 2 The Elemental Mapping Image of the $Ni_{0.5}Fe_{0.5}$@C

The phase structures of the samples were analyzed using XRD. Figure 3(a) displays the XRD patterns of the Ni_xFe_{1-x}@C composites (x = 0.2, 0.4, 0.5, 0.6, and 0.8). Three distinct diffraction peaks are observed at 2θ values of 43.8°, 51.2°, and 75.3°, which correspond to the (111), (200), and (220) crystal planes of the NiFe alloy (JCPDS No. 12-0736), respectively. Furthermore, the relative intensities of these diffraction peaks are consistent with the standard card. These results indicate that the NiFe alloy composites were successfully obtained following the pyrolysis of the Ni_xFe_{1-x}-MOF precursors. Notably, a slight shift of the diffraction peaks toward higher angles is observed with increasing Ni content. This shift suggests the occurrence of lattice distortion and a decrease in the interplanar spacing, which can be attributed to the smaller atomic radius of Ni compared to that of Fe.

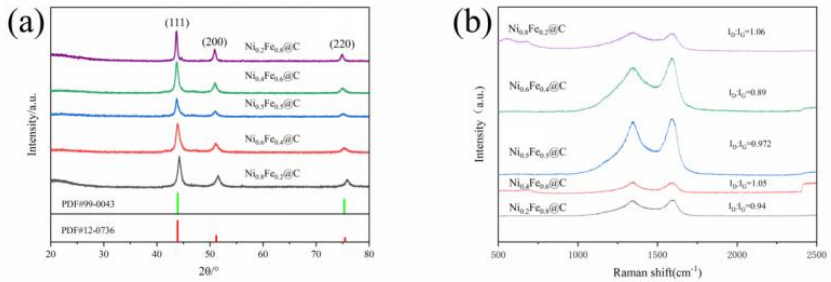

Figure 3 (a)XRD Pattern of Ni_xFe_{1-x}@C Composites, (b)Raman Spectra of Ni_xFe_{1-x}@C Composites

MOF derivatives possess a carbon skeleton structure similar to that of carbon-based materials. Their microwave absorption capacity is closely related to the characteristic structure of carbon, which can be analyzed via Raman spectroscopy[27]. As shown in Figure 3(b), all samples exhibit two distinct peaks in the range of 1000–2000 cm^{-1}: a broad peak at approximately 1350 cm^{-1} (D-band) and a relatively sharp peak at approximately 1590 cm^{-1} (G-band). Generally, the D-band represents the vibration of sp^3 atoms in disordered graphite, while the G-band corresponds to the in-plane vibration of sp^2 atoms in a two-dimensional hexagonal lattice. The I_D / I_G intensity ratio indicates the degree of graphitization of the material. The I_D / I_G values for $Ni_{0.2}Fe_{0.8}$@C, $Ni_{0.4}Fe_{0.6}$@C, $Ni_{0.5}Fe_{0.5}$@C, $Ni_{0.6}Fe_{0.4}$@C and $Ni_{0.8}Fe_{0.2}$@C are 0.94, 1.05, 0.972, 0.89, and 1.06, respectively. It can be inferred that the carbon skeleton gradually transforms from amorphous carbon to graphitic crystals during the sintering process. The enhanced I_D / I_G ratios suggest the presence of defects and disordered carbon. These carbon defects, induced by doping, contribute to microwave absorption through defect polarization. Furthermore, the results indicate that all samples exhibit a favorable degree of graphitization, containing sufficient graphitic carbon to facilitate electron transport. This characteristic enhances the conduction loss capacity of the microwave absorbing materials, thereby improving their overall microwave absorption performance.

The surface chemical states of the $Ni_{0.5}Fe_{0.5}$@C material were investigated using XPS. The survey spectrum in Figure 4(a) confirms the presence of C, N, O, Ni, and Fe elements. The sample primarily consists of Ni, Fe, and C. The N element originates from surface-adsorbed nitrogen, while the O element is attributed to adsorbed oxygen, carbon dioxide, or the natural oxidation of the metal surface. Figure 4(b) presents the high-resolution C 1s spectrum and its deconvolution results, revealing the presence of C=O (285.95 eV) and C–C/C=C (283.59 eV) bonds. The dominance of C–C/C=C bonds is consistent with previous reports [28], along with some adsorbed carbon oxides on the surface. In the Fe 2p spectrum (Figure 4(c)), the peak at 706.5 eV represents metallic Fe (Fe^0), the peak at 710.7 eV represents oxidized Fe on the surface, while the remaining peaks correspond to Fe $2p_{1/2}$ or satellite peaks. Similarly, the Ni 2p spectrum (Figure 4(d)) shows a peak at 851.89 eV corresponding to metallic Ni (Ni^0), with the other peaks attributed to Ni^{2+}, likely resulting from surface oxidation in air. These findings are in good agreement with the XRD results, confirming that the obtained samples are NiFe alloys. Combined with the carbon analysis, these results demonstrate the successful synthesis of the Ni_xFe_{1-x}@C composite.

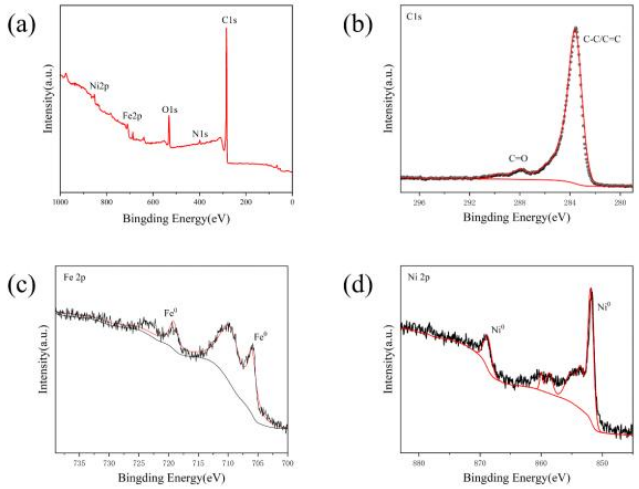

Figure 4 XPS Spectra of $Ni_{0.5}Fe_{0.5}$@C

The microwave absorption capacity of the Ni_xFe_{1-x}@C composites was evaluated by calculating the reflection loss (RL) values based on the transmission line theory. The RL values were determined according to Equation (1). Figures 5(a–e) illustrate the microwave absorption results for samples $Ni_{0.2}Fe_{0.8}$@C, $Ni_{0.4}Fe_{0.6}$@C, $Ni_{0.5}Fe_{0.5}$@C, $Ni_{0.6}Fe_{0.4}$@C, and $Ni_{0.8}Fe_{0.2}$@C, respectively. For each sample, the results are presented as three-dimensional (3D) RL surfaces, two-dimensional (2D) RL contour maps, and RL curves. Notably, the $Ni_{0.5}Fe_{0.5}$@C composite exhibited a maximum RL value of -81.35 dB at 13.8 GHz with a matching thickness of 1.94 mm, and the corresponding effective absorption bandwidth (EAB, RL < -10 dB) reached 5.3 GHz (11.7–17.0 GHz). For the $N_{0.8}Fe_{0.2}$@C sample, a maximum RL of

-50.2 dB was achieved at 14.2 GHz with a thickness of 2.0 mm, yielding an EAB of 5.3 GHz (12.7–18.0 GHz). In contrast, the other samples did not exhibit significant microwave absorption capabilities.

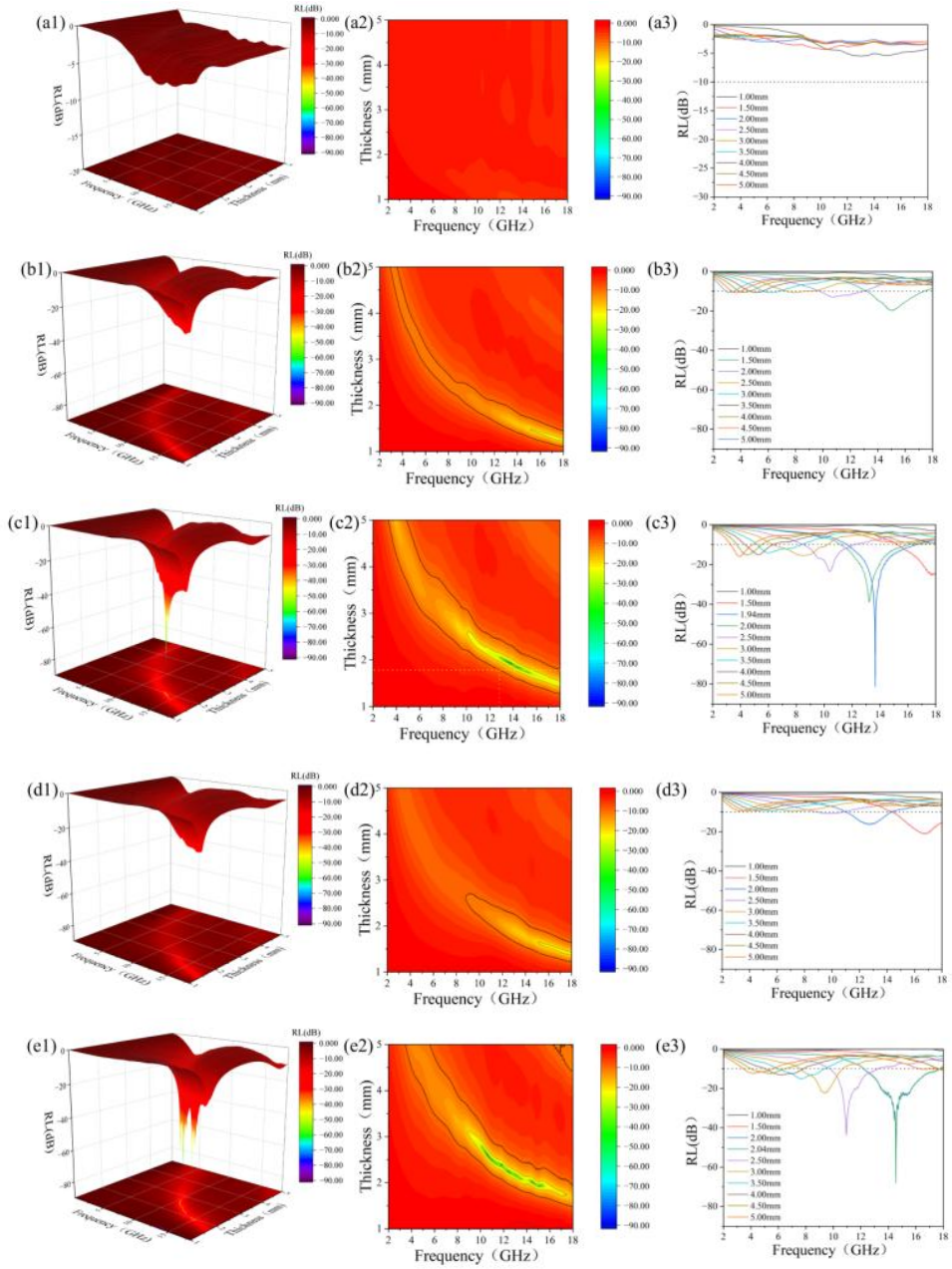

Figure 5 Digital (1)3D RL curves, (2) 2D contour maps and (3) RL-d curves of (a)$Ni_{0.2}Fe_{0.8}$@C, (b)$Ni_{0.4}Fe_{0.6}$@C, (c)$Ni_{0.5}Fe_{0.5}$@C, (d)$Ni_{0.6}Fe_{0.4}$@C, and (e)$Ni_{0.8}Fe_{0.2}$@C

Figures 6(a), (b), and (c) present the results for the complex permittivity, complex permeability, and loss tangents of the samples. The frequency-dependent trends of the real part (ε′) and imaginary part (ε″) of the permittivity are shown in Figures 6(a) and 6(b). Overall, both ε′ and ε″ values exhibit a gradual decline with increasing frequency, which is consistent with the frequency-dependent dielectric dispersion behavior [29-30]. The ε′ values for Ni_xFe_{1-x}@C (x = 0.2, 0.4, 0.5, 0.6, 0.8) range from 58.8–17.2, 18.4–10.5, 12.8–6.8, 17.0–8.3, and 11.4–7.1, respectively. This downward trend indicates that dipoles struggle to respond rapidly to the alternating electric field at higher frequencies, leading to a decrease in permittivity. Minor fluctuations observed in the ε′ and ε″ curves reflect heterogeneous polarization effects caused by local inhomogeneities within the material. In the 12–18 GHz range, multiple resonance peaks appear in the dielectric loss tangent ($\tan\delta_\varepsilon$) curves for all samples. These peaks are primarily attributed to the synergistic effects of the carbon layers, alloy particles, and multiple interfaces, which enhance interfacial polarization, conduction loss, and dipole polarization. Notably, the dielectric loss of $Ni_{0.5}Fe_{0.5}$@C is significantly higher than that of the other samples.
Figures 6(d) and 6(e) illustrate the variations in the real part (μ′) and imaginary part (μ″) of the permeability. Due to the ferromagnetic characteristics of Ni_xFe_{1-x}@C, both μ′ and μ″ exhibit fluctuating trends within the 2–18 GHz range. The μ′ values for Ni_xFe_{1-x}@C (x = 0.2, 0.4, 0.5, 0.6, 0.8) range from 1.23–1.22, 1.40–1.08, 1.41–1.27, 1.43–1.00, and

1.43–0.97, respectively. As a magnetic material, NiFe generates magnetic loss under the influence of electromagnetic waves.

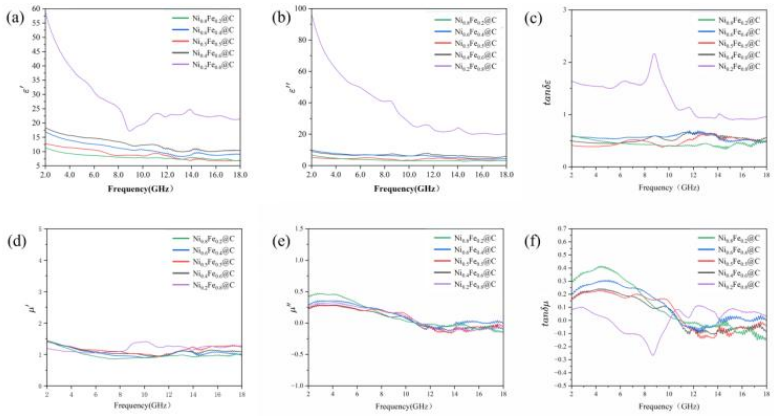

Figure 6 Electromagnetic Parameters of the Ni_xFe_{1-x}@C Composites: ε'(a), ε''(b), tanδε(c), μ'(d), μ''(e) and $tan\delta_\mu$(f)

The μ′ values exhibit a trend of initially decreasing and then increasing with frequency, with distinct resonance peaks observed around 11 GHz and 16 GHz. This indicates that both natural resonance and exchange resonance contribute to the magnetic loss mechanism. The μ″ values of the five samples show minimal differences, with the magnetic loss capacity following the order: $Ni_{0.8}Fe_{0.2}$@C > $Ni_{0.6}Fe_{0.4}$@C > $Ni_{0.2}Fe_{0.8}$@C > $Ni_{0.5}Fe_{0.5}$@C ≈ $Ni_{0.4}Fe_{0.6}$@C. Notably, negative μ″ values are observed for some samples, a phenomenon commonly reported in highly conductive materials. These negative values primarily reflect eddy current losses and magnetic resonance effects, serving as a manifestation of magnetic loss. The underlying mechanism involves induced currents within the material generating a reverse magnetic field that partially offsets the external field, resulting in a negative effective permeability [31]. Figures 6(c) and 6(f) depict the frequency dependence of $tan\delta_\varepsilon$ and $tan\delta_\mu$, respectively. For all samples, the $tan\delta_\varepsilon$ values are significantly higher than the $tan\delta_\mu$ values, indicating that microwave absorption is predominantly governed by dielectric loss [32-33]. This is mainly attributed to the introduction of multiple interfaces, which significantly enhances conduction loss, dipole polarization, and interfacial polarization. Furthermore, the dielectric loss becomes more prominent in the high-frequency range, confirming the role of multiple interfaces in promoting high-frequency polarization. The appearance of negative magnetic loss tangent values at high frequencies may be due to the eddy current effect induced by the external electromagnetic field, leading to an increase in magnetic energy. According to the law of conservation of energy, an increase in magnetic energy must be accompanied by a decrease in electric field energy, implying an enhancement of dielectric loss in this frequency band. This is consistent with the previous analysis of permittivity and permeability. The samples exhibit significantly higher $tan\delta_\varepsilon$ values, which is closely related to their abundant multi-interface structures that induce strong conduction loss and polarization effects, demonstrating superior dielectric loss performance.

Generally, Debye relaxation can be represented by Cole–Cole semicircles, which explain the dielectric behavior of samples across different frequencies [34]. According to Debye theory, the relative complex permittivity (ε_r) can be derived as follows:

$$\left(\varepsilon' - \frac{\varepsilon_s - \varepsilon_\infty}{2}\right)^2 + (\varepsilon'')^2 = \left(\frac{\varepsilon_0 - \varepsilon_\infty}{2}\right)^2 \quad (2)$$

To investigate the polarization loss mechanisms, the Cole–Cole plots of the Ni_xFe_{1-x}@C composites are presented in Figure 7, where each semicircle corresponds to a Debye polarization relaxation process. All five samples exhibit multiple irregular semicircles, indicating the occurrence of multiple polarization relaxation processes and diverse dielectric loss mechanisms. The charge accumulation at the heterogeneous interfaces between the NiFe particles and the carbon matrix likely leads to interfacial polarization. Furthermore, oxygen-containing functional groups in the carbon material (e.g., C=O and C–O) can serve as polarization centers to induce dipole polarization. The straight lines observed at the end of the Cole–Cole plots for all five samples indicate that conduction loss also contributes to the electromagnetic wave attenuation. Specifically, the NiFe nanoparticles, as metallic components, possess inherent electrical conductivity that manifests as conduction loss. Additionally, the micro-conductive networks within the carbon framework further contribute to the overall conduction loss.

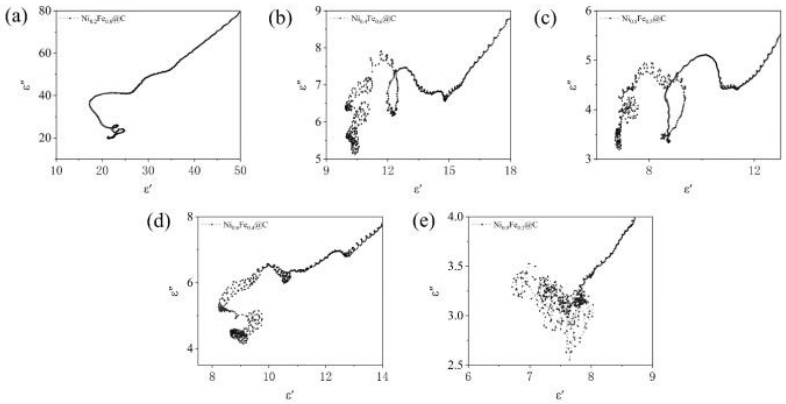

Figure 7 Cole-Cole Semicircles of P1 (a)$Ni_{0.2}Fe_{0.8}$@C, (b)$Ni_{0.4}Fe_{0.6}$@C, (c)$Ni_{0.5}Fe_{0.5}$@C, (d)$Ni_{0.6}Fe_{0.4}$@C, and (e)$Ni_{0.8}Fe_{0.2}$@C

Impedance matching determines the absorption capacity of microwave absorbing materials for electromagnetic waves. The evaluation of the electromagnetic impedance matching degree is expressed by Equation (3) [35]:

$$|\Delta| = \quad |\sinh 2(Kfd) - M \quad | \tag{3}$$

Where K and M are determined by the complex permittivity (ε_r) and complex permeability (μ_r). A smaller |Δ| value (especially a larger area satisfying |Δ| < 0.4) indicates better impedance matching of the material. According to this criterion, when the |Δ| value is significantly greater than zero, the electromagnetic wave absorption performance will decrease markedly. Figures 8(a)–(e) illustrate the impedance matching degrees of the five samples under various frequency and thickness conditions. It can be observed that for $Ni_{0.2}Fe_{0.8}$@C, $Ni_{0.4}Fe_{0.6}$@C, and $Ni_{0.6}Fe_{0.4}$@C, the |Δ| values are significantly greater than 0.4 over most of the range, indicating unsatisfactory impedance matching, which is consistent with their low reflection loss. In contrast, $Ni_{0.5}Fe_{0.5}$@C and $Ni_{0.8}Fe_{0.2}$@C exhibit larger areas where |Δ| < 0.4. Specifically, $Ni_{0.5}Fe_{0.5}$@C shows favorable impedance matching in the thickness range of 1.5–3 mm and frequency range of 5–18 GHz, which is in good agreement with its microwave absorption results. Additionally, $Ni_{0.8}Fe_{0.2}$@C demonstrates good impedance matching in the thickness range of 1–4 mm and frequency range of 5–12 GHz. These findings align with the microwave absorption results, where $Ni_{0.5}F_{0.5}$@C achieves the strongest absorption at 13.8 GHz with a thickness of 1.94 mm, and $Ni_{0.8}Fe_{0.2}$@C shows the strongest absorption near 11 GHz with a thickness of 2.5 mm. This indicates that impedance matching plays a dominant role in the microwave absorption of these samples.

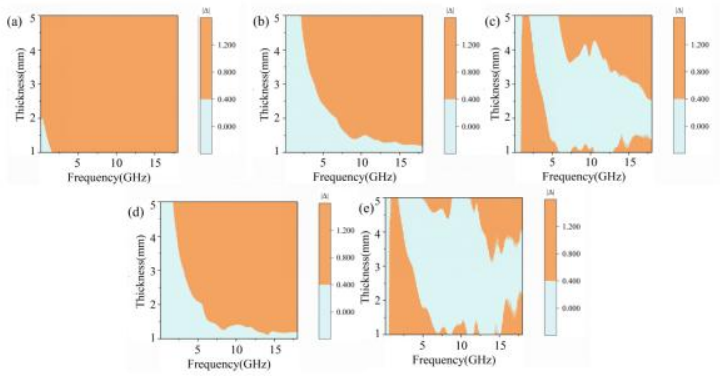

Figure 8 The Impedance Matching Degree Diagram of the Composite Material, (a)$Ni_{0.2}Fe_{0.8}$@C, (b)$Ni_{0.4}Fe_{0.6}$@C, (c)$Ni_{0.5}Fe_{0.5}$@C, (d)$Ni_{0.6}Fe_{0.4}$@C, and (e)$Ni_{0.8}Fe_{0.2}$@C

Furthermore, according to electromagnetic wave transmission theory, the attenuation constant (α) is commonly employed to characterize the electromagnetic loss per unit length of electromagnetic waves within a material [36], which can be expressed by Equation (4):

$$\alpha = \frac{\pi f\sqrt{2}}{c}\sqrt{\left(\varepsilon''\mu'' - \varepsilon'\mu'\right) + \sqrt{(\varepsilon''\mu'' - \mu'\varepsilon')^2 + (\mu'\varepsilon'' + \mu''\varepsilon')^2}} \tag{4}$$

Where f represents the frequency and c denotes the speed of light. A higher attenuation constant value indicates a stronger attenuation capability of the material for electromagnetic waves. Figure 9 displays the frequency-dependent attenuation constant curves for the samples. It can be observed that all samples exhibit relatively high attenuation constant values, suggesting strong electromagnetic wave dissipation capabilities. Furthermore, the attenuation constant increases with frequency, indicating enhanced loss capacity in the high-frequency range. Within the 2–18 GHz range, the attenuation capacity of the five samples follows the order: $Ni_{0.2}Fe_{0.8}$@C>$Ni_{0.4}Fe_{0.6}$@C>$Ni_{0.6}Fe_{0.4}$@C >$Ni_{0.5}Fe_{0.5}$@C >$Ni_{0.8}Fe_{0.2}$@C. Notably, although the $Ni_{0.5}Fe_{0.5}$@C composite exhibits the best microwave absorption performance, its attenuation constant is relatively small. This is primarily because $Ni_{0.5}Fe_{0.5}$@C possesses the optimal impedance matching in the high-frequency range. In contrast, while

$Ni_{0.6}Fe_{0.4}$@C and $Ni_{0.4}Fe_{0.6}$@C have larger attenuation constants, their poor impedance matching prevents them from achieving superior microwave absorption performance. This underscores the critical role of impedance matching in this system. The optimal microwave absorption performance of a sample is the result of the synergistic effect between impedance matching and attenuation loss.

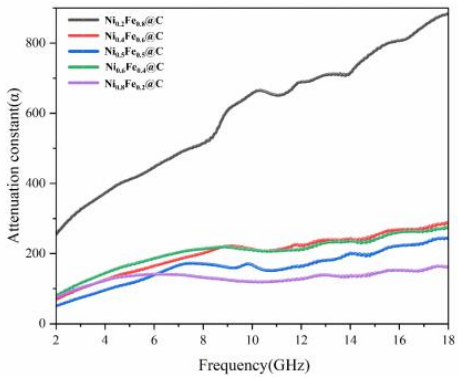

Figure 9 The Attenuation Constant of the Ni_xFe_{1-x}@C Composites

4 CONCLUSION

In summary, the Ni_xFe_{1-x}@C composites with diverse morphologies were successfully fabricated from Ni_xFe_{1-x}-MOF precursors by simply adjusting the Ni/Fe molar ratios (0.2:0.8, 0.4:0.6, 0.5:0.5, 0.6:0.4, and 0.8:0.2). Among the obtained Ni_xFe_{1-x}@C composites, the octahedral $Ni_{0.5}Fe_{0.5}$@C structure exhibited superior microwave absorption performance in terms of both maximum reflection loss intensity and the corresponding effective absorption bandwidth (EAB). Specifically, the composite achieved a minimum reflection loss (RL_{min}) of -81.35 dB and an EAB (RL < -10 dB) of 5.3 GHz. The optimal microwave absorption performance of the sample is the result of the synergistic effect between impedance matching and attenuation loss. Both the optimized composition and the porous hollow structure contributed to these exceptional microwave absorption properties. Consequently, the as-prepared Ni_xFe_{1-x}@C composites hold great promise for practical applications in the field of microwave absorbing materials.

COMPETING INTERESTS

The authors have no relevant financial or non-financial interests to disclose.

REFERENCES

[1] Zhang Y, Huang Y, Zhang TF, et al. Broadband and tunable high-performance microwave absorption of an ultralight and highly compressible graphene foam. Advanced Materials, 2015, 27(12): 2049-2053.
[2] Fan G, Jiang Y, Xin J, et al. Facile synthesis of Fe@Fe3C/C nanocomposites derived from bulrush for excellent electromagnetic wave-absorbing properties. ACS Sustainable Chemistry & Engineering, 2019, 7(23): 18765-18774.
[3] Sun H, Che RC, You X, et al. Cross-stacking aligned carbon-nanotube films to tune microwave absorption frequencies and increase absorption intensities. Advanced Materials, 2014, 26(48): 8120-8125.
[4] Dong XL, Zhang XF, Huang H, et al. Enhanced microwave absorption in Ni/polyaniline nanocomposites by dual dielectric relaxations. Applied Physics Letters, 2008, 92(1): 013127.
[5] Che RC, Peng LM, Duan XF, et al. Microwave absorption enhancement and complex permittivity and permeability of Fe encapsulated within carbon nanotubes. Advanced Materials, 2004, 16(5): 401-405.
[6] Zhang X, Qiao J, Jiang YY, et al. Carbon-based MOF derivatives: emerging efficient electromagnetic wave absorption agents. Nano-Micro Letters, 2021, 13: 135.
[7] Shu JC, Cao WQ, Cao MS, et al. Diverse metal-organic framework architectures for electromagnetic absorbers and shielding. Advanced Functional Materials, 2021, 31(23): 2100470.
[8] Dai SS, Cheng Y, Quan B, et al. Porous-carbon-based Mo2C nanocomposites as excellent microwave absorbers: a new exploration. Nanoscale, 2018, 10(15): 6945-6953.
[9] Xiang Z, Song YM, Xiong J, et al. Enhanced electromagnetic wave absorption of nanoporous Fe3O4@carbon composites derived from metal-organic frameworks. Carbon, 2019, 142: 20-31.
[10] Miao P, Zhou R, Chen KJ, et al. Tunable electromagnetic wave absorption of supramolecular isomer-derived nanocomposites with different morphology. Advanced Materials Interfaces, 2020, 7(4): 1901820.
[11] Ye YX, Ma ZL, Lin RB, et al. Pore space partition within a metal-organic framework for highly efficient C2H2/CO2 separation. Journal of the American Chemical Society, 2019, 141: 4130-4136.
[12] Zeng QW, Wang L, Li X, et al. Double ligand MOF-derived pomegranate-like Ni@C microspheres as high-performance microwave absorber. Applied Surface Science, 2021, 538: 148051.

[13] Quan B, Shi WH, Lu XC, et al. Defect engineering in two common types of dielectric materials for electromagnetic absorption applications. Advanced Functional Materials, 2019, 29(28): 1901236.
[14] Wang L, Huang MQ, Yu XF, et al. MOF-derived Ni1-xCox@carbon with tunable nano-microstructure as lightweight and highly efficient electromagnetic wave absorber. Nano-Micro Letters, 2020, 12: 150-166.
[15] Shu RW, Li XH, Tian KH, et al. Fabrication of bimetallic metal-organic frameworks derived Fe3O4/C decorated graphene composites as high-efficiency and broadband microwave absorbers. Composites Part B, 2022, 228: 109423.
[16] Tao JQ, Xu LL, Jin HS, et al. Selective coding dielectric genes based on proton tailoring to improve microwave absorption of MOFs. Advanced Powder Materials, 2023, 2: 100091.
[17] Huang LN, Liu XF, Chuai D, et al. Flaky FeSiAl alloy-carbon nanotube composite with tunable electromagnetic properties for microwave absorption. Scientific Reports, 2016, 6: 35377.
[18] Wei T, Zhang XZ, Gou Y, et al. Hybrid silica-carbon bilayers anchoring on FeSiAl surface with bifunctions of enhanced anti-corrosion and microwave absorption. Carbon, 2021, 173: 185-193.
[19] Ma L, Li SZ, Liu FC, et al. Metal-organic framework derived Co/C composite with high magnetization as broadband electromagnetic wave absorber. Journal of Alloys and Compounds, 2022, 906: 164257.
[20] Wang L, Wen BO, Bai X, et al. NiCo alloy/carbon nanorods decorated with carbon nanotubes for microwave absorption. ACS Applied Nano Materials, 2019, 2(12): 7827-7838.
[21] Huang L, Huang S, Yang Z, et al. In-situ conversion of ZnO/Ni3ZnC0.7/CNT composite from NiZn bimetallic MOF precursor with enhanced electromagnetic property. Nanomaterials, 2018, 8: 600.
[22] Shu RW, Li XH, Ge CQ, et al. Synthesis of FeCoNi/C decorated graphene composites derived from trimetallic metal-organic framework as ultrathin and high-performance electromagnetic wave absorbers. Journal of Colloid and Interface Science, 2023, 630: 754-762.
[23] Wang L, Wen B, Yang HB, et al. Hierarchical nest-like structure of Co/Fe MOF derived CoFe@C composite as wide-bandwidth microwave absorber. Composites Part A, 2020, 135: 105958.
[24] Shu RW, Li XH, Shi JJ, et al. Construction of porous carbon-based magnetic composites derived from iron zinc bimetallic metal-organic framework as broadband and high-efficiency electromagnetic wave absorbers. Journal of Colloid and Interface Science, 2023, 633: 43-52.
[25] Shu RW, Li WJ, Wu Y, et al. Nitrogen-doped Co-C/MWCNTs nanocomposites derived from bimetallic metal-organic frameworks for electromagnetic wave absorption in the X-band. Chemical Engineering Journal, 2019, 362: 513-524.
[26] Shu R, Zhang G, Wang X, et al. Fabrication of 3D net-like MWCNTs/ZnFe2O4 hybrid composites as high-performance electromagnetic wave absorbers. Chemical Engineering Journal, 2018, 337: 242-252.
[27] Wang FY, Wang N, Han XJ, et al. Core-shell FeCo@carbon nanoparticles encapsulated in polydopamine derived carbon nanocages for efficient microwave absorption. Carbon, 2019, 145: 701-711.
[28] Dai SS, Cheng Y, Quan B, et al. Porous-carbon-based Mo2C nanocomposites as excellent microwave absorber: a new exploration. Nanoscale, 2018, 10: 6945-6953.
[29] Dong J, Lin Y, Zong H, et al. Three-dimensional architecture reduced graphene oxide – LiFePO4 composite: preparation and excellent microwave absorption performance. Inorganic Chemistry, 2019, 58(3): 2031-2041.
[30] Lin Y, Li D, Zhang M, et al. (Na0.5Bi0.5)0.7Sr0.3TiO3 modified by Bi(Mg2/3Nb1/3)O3 ceramics with high energy-storage properties and an ultrafast discharge rate. Journal of Materials Chemistry C, 2020, 8(7): 2258-2264.
[31] Deng L, Han M. Microwave absorbing performances of multiwalled carbon nanotube composites with negative permeability. Applied Physics Letters, 2007, 91(2): 023119.
[32] Rao L, Wang L, Yang C, et al. Confined diffusion strategy for customizing magnetic coupling spaces to enhance low-frequency electromagnetic wave absorption. Advanced Functional Materials, 2023, 33(16).
[33] Sun Y, Zhong W, Wang Y, et al. MoS2-based mixed-dimensional van der Waals heterostructures: a new platform for excellent and controllable microwave-absorption performance. ACS Applied Materials & Interfaces, 2017, 9(39): 34243-34255.
[34] Fan H, Yao Z, Zhou J, et al. Enhanced microwave absorption of epoxy composite by constructing 3D Co–C–MWCNTs derived from metal-organic frameworks. Journal of Materials Science, 2021, 56(2): 1426-1442.
[35] He L, Zhao Y, Xing L, et al. Preparation of reduced graphene oxide coated flaky carbonyl iron composites and their excellent microwave absorption properties. RSC Advances, 2018, 8(6): 2971-2977.
[36] Dong S, Zhang X, Zhang W, et al. A multiscale hierarchical architecture of SiC whiskers – graphite nanosheets/polypyrrole ternary composite for enhanced electromagnetic wave absorption. Journal of Materials Chemistry C, 2018, 6: 10804-10814.